Biomimetic Silk Macroporous Materials for Drug Delivery Obtained via Ice-Templating

Kankan Qin, Rui Pereira, Thibaud Coradin, Verónica de Zea Bermudez, Francisco M. Fernandes

Biomimetic silk macroporous materials for drug delivery obtained via ice templating

Kankan Qin[1], Rui F.P. Pereira[2], Thibaud Coradin[1], Verónica de Zea Bermudez[3], Francisco M. Fernandes[1]**

[1] Sorbonne Université, UMR 7574, Laboratoire de Chimie de la Matière Condensée de Paris, F-75005, Paris, France

[2] Chemistry Center and Chemistry Department, University of Minho, Campus de Gualtar, 4710-057, Braga, Portugal

[3] Chemistry Department and CQ-VR, University of Trás-os-Montes e Alto Douro, Apartado 1013, 5001-801, Vila Real, Portugal

KEYWORDS: Ice templating, Macroporous materials, Silk, Fibroin, Sericin, Drug delivery

ABSTRACT

Silk from *Bombyx mori* is one of the most exciting materials in Nature. The apparently simple arrangement of its two major components—two parallel filaments of silk fibroin (SF) coated by a common sericin (SS) sheath—provides a combination of mechanical and surface properties able to protect the moth during its most vulnerable phase, the pupal stage. Here, we recapitulate the topology of native silk fibers but shape them into three-dimensional porous constructs using an unprecedented design strategy. We demonstrate, for the first time, the potential of these macroporous silk foams as dermal patches for wound protection and for the controlled delivery of Rifamycin (Rif), a model antibiotic. The method implies: *i)* removing SS from silk fibers; *ii)* shaping SF solutions into macroporous foams via ice-templating; *iii)* stabilizing the SF macroporous in a methanolic solution of Rif; *iv)* coating Rif-loaded SF foams with a SS sheath. The resulting SS@SF foams exhibit water wicking capacity and accommodate up to ~20% deformation without detaching from a skin model. The antibacterial behavior of Rif-loaded SS@SF foams against *Staphylococcus aureus* on agar plate outperforms that of SF foams (>1 week and 4 days, respectively). The re-assembly of natural materials as macroporous foams—illustrated here for the reconstruction of silk-based materials—can be extended to other multicomponent natural materials and may play an important role in applications where controlled release of molecules and fluid transport are pivotal.

INTRODUCTION

In Nature, porosity—pore size distribution, pore geometry, and connectivity—plays a critical role in many materials. In particular, interconnected macroporosity modulates the interactions with cells, determines the liquid transport mechanisms, and regulates the overall mechanics of natural materials. Trabecular bone—the porous fraction of bone composed of an interconnected network of trabeculae—stands out as a paradigm of the tremendous benefits arising from a finely controlled macroporous structure;[1] but also wood[2], coral,[3] or the frustule in diatoms[4] are just as good examples, illustrating the central role of porosity in combining mechanics and liquid transport in natural materials.

Devising new ways to shape biomolecules into macroporous constructs, that reproduce the structural motifs and composition found in natural materials, holds promise in dictating their functionalities in applications such as drug delivery carriers, biomimetic membranes, acoustic systems, and implants.[5] In this context, ice-templating offers a simple yet versatile route to fabricate aligned macroporous biomaterials from biopolymers.[6–10] The technique, which has evolved mainly in the ceramics materials community, is based on a uniaxial thermal gradient that promotes the segregation of solutes and/or suspended particles induced by a growing ice front. Since the solubility of most molecular species in ice is extremely limited, the freezing step forces solutes to progressively accumulate in between the growing ice crystals. Sublimation then reveals the material's macroporous structure defined by ice growth, a fingerprint of the thermal boundaries imposed during the freezing step.

In this work we propose an original approach to fabricate silk foams using ice-templating in which we reproduce both silk's native composition and topological assembly between its components. Silk threads are characterized by a silk sericin SS envelope surrounding two parallel

silk fibroin (SF) brins. Our strategy relies on the controlled disassembly and re-assembly of the two silk proteins. It involves the removal of the outer component (SS), followed by shaping of the core component (SF) via ice-templating which is finally covered with SS to yield a reconstructed silk foam (SS@SF) whose application as a dermal patch is demonstrated (Figure 1). In practice, our design strategy couples top-down structuration (SS removal) and bottom-up assembly (SF ice templating followed by SS coating) to engineer a functional material with improved features. Two reasons motivated the development of SS@SF-based dermal patches. The first is that SF foams have been previously proposed for the fabrication of biocompatible three-dimensional (3D) aligned scaffolds for tissue engineering applications, due to the scaffolds' ability to promote cell contact guiding.[9,10] However, beyond cell guiding, the aligned macroporous channels generated by ice-templating also configure an effective capillary transport system[13]—as compared to randomly oriented pores—that could be beneficial for the clearance of exudates between the wound and the patch external surface during healing. The second reason is that, to the best of our knowledge, dermal patches in which SF and SS coexist have not been reported to date.[11,14] Because of the different hydrophobic/hydrophilic balance of both proteins, and due to their close and efficient association in native silk, these materials may provide an invaluable platform to control drug release in biological settings.

Using porous silk materials is particularly attractive in wound healing[15] due to suitable cell attachment and migration both *in vitro*[16] and *in vivo*[17] but also in clinical application such as the abdominal wall fascial reinforcement[18]. As noted above, silk-based wound dressing materials have been solely built from degummed (SS-free) silk. SS's largely accepted immunogenic role has limited the development of SS-containing silk materials for biomedical applications.[19] This shortcoming has been, however, challenged over the past decade with a growing body of work

both in academic and clinical contexts where the potential of SS has been emphasized.[20–24] The confusion regarding the role of SS in eliciting an immune response is now mostly attributed to the native silk threads rather than their individual major components.[25] Combining recent knowledge on SS with the widely explored solution processing routes to fabricate SF materials opens an interesting pathway to redesign new silk-based biomaterials able to reproduce the topology of the natural material based on its two major components.[26]

The constructs produced here were obtained via a four-step process (Figure 1): *i) Bombyx Mori* silk degumming; *ii)* ice-templating of aqueous SF solution, ensuring a controlled anisotropic macroporous structure; *iii)* methanol (MeOH)-induced enhancement of the β-sheet domain content of SF; and *iv)* coating of SF with a SS sheath to yield a reconstructed 3D macroporous silk material. The SS@SF core-shell system obtained represents a suitable 3D cage to encapsulate and deliver Rifamycin (Rif), a bactericidal hydrophilic molecule that works by binding to—and inhibiting—the DNA-dependent RNA polymerase.[27]

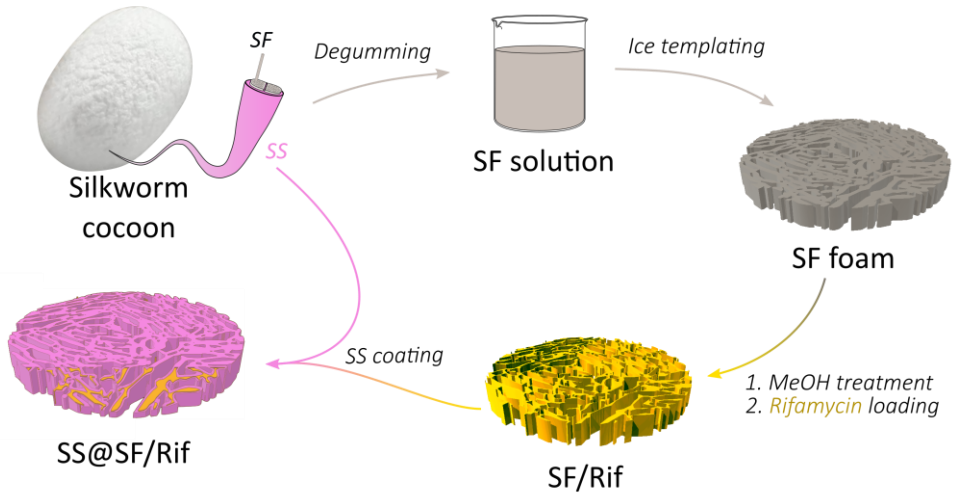

Figure 1. Simplified scheme for the fabrication of SS@SF/Rif foams. Following degumming, SF solution is structured into a macroporous foam via ice templating. Upon MeOH stabilization

and Rif loading, the resulting foams are covered with a SS sheath, recapitulating the initial concentric organization of native silk.

The present SS@SF platform was tested as an antibiotic delivery system under the form of temporary disk patches, an attractive vector for the delivery of topical drugs.[28,29] We took advantage of the MeOH stabilization step to load SF foams with Rif before coating the foam with the SS sheath. Loading the patches with Rif during MeOH treatment presents the advantage of minimizing Rif desorption during the stabilization step of SF, as compared to preloading with Rif prior to stabilization. As-produced SS@SF foams show liquid wicking properties, an important property to keep wounds clear from exudates during healing. The SS coating helps to retain more Rif and the freezing rate for foam fabrication tunes its release kinetics in aqueous solution. Long-term antibacterial activity on agar plate nominates these novel silk matrices as good candidates for developing antibacterial dermal patches which could find application in the prevention and treatment of chronic wounds, such as neuropathic,[30] venous,[31] pressure,[32] and diabetic,[33] ulcers, which affect millions of patients each year.

EXPERIMENTAL

Materials. *Bombyx mori L.* cocoons were supplied by APPACDM (Castelo Branco, Portugal). Silk sericin for cell culture from *Bombyx Mori* was purchased from SIGMA-ALDRICH (SS, ref. S5201, UNIPROT references A8CEQ1 and D2WL76), Sodium carbonate (Na_2CO_3, Sigma-Aldrich, ≥ 99%), lithium bromide (LiBr, Fluka, > 99%), Rhodamine-B isothiocyanate (RITC, SIGMA-ALDRICH, > 80%), N,N-dimethylformamide (DMF, SIGMA-ALDRICH, 99.8%), Rifamycin SV sodium salt (Rif, SIGMA-ALDRICH, >900 units/mg) and methanol (MeOH, Acros Organics, ≥ 99.8%, ACS reagent) were used as received.

Methods. *Preparation of SF aqueous solution.* Preparation and purification of SF was performed according to the protocol previously reported.[26] *B. mori* cocoons (5.0 g) were cut into small pieces and boiled for 30 min in a 0.02 M Na_2CO_3 solution to induce degumming. The resulting fibers were subsequently rinsed several times with distilled water, squeezed out to remove the excess water, and dried overnight in a fume hood. SF was immersed into 9.3 M LiBr solution (ratio, 1 g: 4 mL) and then incubated at 60 °C for 4 h. SF solution was dialyzed against ultrapure water for 48 hours using a 3.5 kDa dialysis membrane (ThermoFisher Scientific). The final SF solution was recovered and stored at 4 °C. Solutions at 2.5, 5.0 and 7.5 wt. % SF aqueous solutions were prepared by dilution from the initial solution.

Fabrication of SF foam. 2.5, 5.0 and 7.5 wt. % of SF solutions were freeze-cast at 1, 10 and 100 °C.min^{-1} using unidirectional freezing home-made setup[13]. Briefly, 2 mL sample solution was poured into a plastic tube fitted onto a temperature-controlled copper rod. A thermal controller was used to precisely control the temperature at the interface between the copper rod and the SF solution. The temperature was stabilized at 20 °C for 3 min, and then decreased to −80 °C at a controlled freezing rate (1, 10 or 100 °C.min^{-1}). Once the temperature reached −80 °C, samples were recovered and freeze-dried (ALPHA 2-4 LD, Christ Martin) for 24 h.

SS-coating of SF foam. Firstly, 100 mL of 10 mg.mL^{-1} SS in carbonate buffer (pH 9.3) was mixed with 1 mL of 1 mg.mL^{-1} of RITC in DMF overnight. The mixture was then dialyzed against ultrapure water with a 3.5 kDa cutoff membrane (ThermoFisher Scientific) for 2 days. Dialysis water was changed every 4 h. RITC-SS was recovered upon freeze-drying the dialyzed solution for 24 h. Prior to SS coating, SF foams (5.0 wt. %, 10 °C.min^{-1}) were immersed in MeOH for 2 h and freeze-dried for 2 h, which resulted in SF-MeOH foams. Subsequently, SS

coated SF foams (SS@SF) were obtained by immersing for 2 h the SF-MeOH foams into 2 wt. % SS/RITC-SS aqueous solution and then drying it at 37 °C in an oven for 24 h.

Scanning Electronic Microscope (SEM). Morphological analysis was performed in a Hitachi S-3400N SEM (Japan) at 10 kV. Scaffolds were cut along and perpendicularly to the main freezing direction and then sputtered with a 10 nm gold layer. Image analysis was performed using FIJI software.

Confocal Microscopy. Second Harmonic Generation of SF non-centrosymmetric structures and fluorescence signal of RITC-SS coating on SF foams were analyzed on a Leica SP5 upright confocal, multiphoton laser scanning microscope to locate the SS distributions inside the foam. Image processing was performed with FIJI software. Co-localization analysis was performed using the Coloc2 plugin that performs Costes[34] auto-threshold analysis to define the signal-rich voxels in each channel followed by Manders[35] and Pearson analysis.[36]

Attenuated Total Reflection Fourier-transform infrared (ATR/FTIR) spectroscopy. SF, SF-MeOH, SS@SF foams were analyzed by FTIR using a PerkinElmer spectrometer 400 with ATR accessories. All ATR/FTIR spectra were recorded in the 4000 to 400 cm^{-1} range by averaging 4 scans and a resolution of 1 cm^{-1}.

Drug Release in Aqueous Solution. SF foams (5.0 wt. %, at 1, 10 and 100 °C.min^{-1}) were directly immersed into 1 mg.mL^{-1} Rif methanolic solution for 2 h and then freeze-dried for 24 h. Half of the samples were subsequently dipped into water for 2 h and the other half in 2 wt. % SS aqueous solution for 2 h. All foams were then dried in an oven at 37 °C. The dried samples were then immersed in 3 mL of water and the release of Rif and proteins were detected at 445 and 280 nm respectively with a UV-vis spectrometer (UVIKONXL SECOMAM). Three replicates were

performed for each condition. The release profile was fitted with three models (Higuchi, Korsmeyer-Peppas, Weibull) in Qtiplot software.

Kirby–Bauer disc diffusion test. 5 wt. % SF scaffolds fabricated at 1, 10 and 100 °C.min^{-1} were immersed into 1 mg.mL^{-1} Rif methanolic solution for 2 h, freeze-dried, and cut into ~1 mm slices. Half of the samples were put into water and the other half in 2 wt. % SS aqueous solution for 2 h. All samples were dried in an oven at 37 °C. The dried slices were placed on the surface of agar culture plate pre-cultured with 10^7 cells.mL^{-1} *Staphylococcus aureus*. The plates were incubated at 30 °C for 24 h and then the inhibition zone was measured. The sample disks were then successively transferred onto a new agar culture plate with pre-cultured bacteria for another 24 h. The inhibition radius was measured daily until no inhibition zone was detected. Data analysis was performed by Graphpad Prism software.

Liquid wicking experiments. SS@SF foams' (5.0 wt. %, prepared at 10 °C.min^{-1}) and SF-MeOH samples' ability to transport water away from the patch/skin interface was determined in a home built setup depicted in the Supplementary Information section (Fig. S1). Briefly a 10 CC Terumo syringe ($\emptyset = 15.8\,mm$), controlled by a syringe pump, was connected to a hypodermic needle piercing a 2 mm silicone substrate where the patch was deposited. The needle tip protruded by 0.5 mm the silicone surface. The foams (diameter of 1.1 cm and thickness of approximately 1 mm) were rehydrated by water immersion prior to the measurements and were deposited on the PDMS surface (over the needle tip). A flow speed of 3 µL.s^{-1} was imposed with the syringe pump to inject water in between the bottom of the sample and the silicone surface. Finally, the volume of water cap above the foam was calculated from the cap height and radius, measured from video analysis on FIJI.

Compliance test. SF and SS@SF foams (5.0 wt. %) fabricated at 1, 10 and 100 °C.min^{-1} were cut into disk-shaped pieces with height of approximately 1 mm. The samples were then immersed for 2 h in water and 2% wt. % SS solution, respectively. Subsequently, wet samples were placed on the surface of a silicone substrate that was stretched to different ratios (5%, 10%, 15%, 20%, 25% and 30%). Relative deformation of the substrate and the sample were measured by video analysis using predefined marks on both the substrate and the sample to infer local strain. Three samples were analyzed for each condition.

RESULTS AND DISCUSSION

Dermal patches fabrication and characterization. Porosity plays a critical role in the performance of antimicrobial dermal patches. It dictates the material's mechanical and liquid transport properties, two key parameters that determine the patch cohesiveness and its ability to extract exudates from the underneath wound. To address the need to fabricate porous patches with a controlled macroporous texture, we performed directional freezing (also called ice-templating or freeze casting) experiments involving different SF solution concentrations and cooling rates. We prepared SF foams from 2.5, 5.0 and 7.5 wt.% SF aqueous solutions at three different cooling rates (1, 10 and 100 °C.min^{-1}). Samples obtained from 2.5 wt.% SF solutions were too fragile to withstand handling and were subsequently discarded from further studies.

Both 5.0 and 7.5 wt. % SF solutions produced foams with lamellar pore morphology, as evidenced in the SEM images obtained from slices cut perpendicular to the ice growth direction (Figure 2A). Both SF concentrations yielded comparable pore sizes, as deduced from the wall-to-wall distance (measured from each pore minimum Feret diameter). As discussed elsewhere, for materials obtained by ice-templating, polymer concentration usually correlates positively with the mechanical properties of otherwise comparable foams.[13] Producing foams whose pore

sections are invariant with the polymer initial concentration allows thus to independently modulate the mechanics of the foams without altering the pore dimensions and thus the materials' liquid transport properties.

The average pore wall-to-wall distances (smallest axis of each pore section) decreased from 90 to 70 μm ([SF] = 5.0 wt. %) and from 100 to 60 μm ([SF] = 7.5 wt. %) with increasing cooling rate (Figure 2B). The full wall-to-wall distance data, obtained by SEM image analysis (N > 180), are plotted next to the boxplots in Figure 2B. These results suggest that it is possible to selectively control the pore size distribution of biopolymer foams by changing SF concentration and cooling rate. Given the comparable morphological properties of the 5.0 and 7.5% SF foams, we have selected the materials obtained from 5.0 wt. % SF aqueous solution for the elaboration of antimicrobial patches.

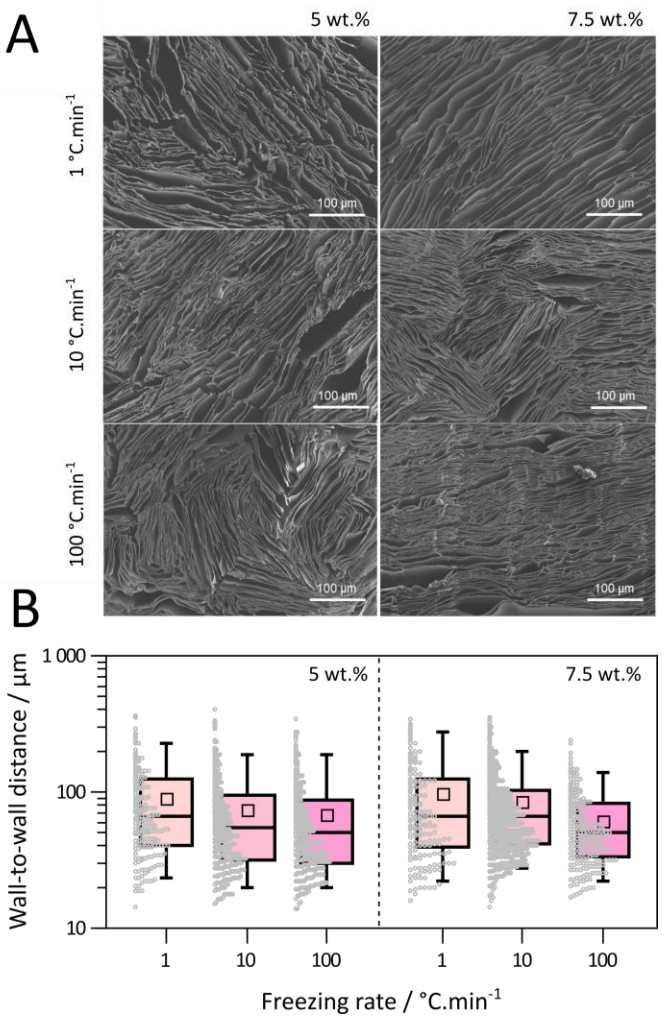

Figure 2 The macroporous structure of ice-templated SF foams is defined by the cooling rate. (A) SEM images of SF foams obtained via ice-templating of 5.0 and 7.5 wt. % SF aqueous solutions at 1, 10 and 100 °C.min^{-1}. (B) Pore wall-to-wall distances determined by analysis of SEM images after thresholding in FIJI software[37]. Boxplots whiskers correspond to the 10th and 90th percentiles, boxpolot upper and lower limits to the 25th and 75th percentile, central line to the median and the average values are plotted with square symbols. The individual data points measured from image analysis are displayed in grey to the left of each boxplot.

Antimicrobial patches work in humid environment, thus requiring the material to be stable in aqueous conditions. Unlike most biomaterials processing routes, ice-templating is particularly useful to preserve the structural and molecular integrity of biopolymers.[6] This feature, commonly considered an advantage to shape temperature-sensitive systems, also means that the intrinsic properties of SF, were not modified during the process and thus that ice-templated SF would dissolve if in contact with water after freeze drying. Owing to the strong hydrogen bonding interactions and hydrophobic nature, β-sheet crystallites favor water insolubility, whereas random coils and α-helices promote water solubility.[38–40] In SF the transformation of random coils into β-sheet structures is facilitated in the presence of MeOH.[41,42] As a consequence, to induce the formation of β-sheets, SF foams were immersed in a MeOH bath at room temperature after freeze-drying. The as-prepared materials preserved the macroporous texture—as demonstrated by SEM (Figure 3A)—where both the pore section aspect ratio and the SF walls' thickness remained unchanged. The formation of additional β-sheet domains was tracked by ATR/FTIR spectroscopy (Figure 3B). The intensity maximum of the broad and non-resolved characteristic amide I band at 1643 cm^{-1} indicates a predominance of random coil conformations in the SF foams. Upon MeOH treatment (SF-MeOH), the maximum intensity shifted to 1625 cm^{-1} and a shoulder emerged at 1699 cm^{-1}. Both spectral features evidence the occurrence of β-sheet structures.[43,44] The stability of SF-MeOH in aqueous media was confirmed by the absence of significant solubility of the foams when soaked in water for at least 4 days (data not shown).

To promote the formation of a reconstructed 3D silk material, the SF-MeOH foams were coated with a SS envelope to mimic silk's native composition and topological arrangement (SS@SF). The obtained SS@SF foams retained the macroporous structure defined through the previous ice-templating and MeOH exposure processing steps, respectively (Figure 3A). The

higher magnification SEM image (right panel, third row of Figure 3A) depicts the foams after SS coating. The walls of the SS@SF foams do not display any noticeable change in thickness when compared to SF-MeOH, suggesting that the SS layer thickness is negligible compared to the SF walls. The characteristic amide I spectroscopic signature of the β-sheet secondary structure is not significantly modified in SS@SF (1623 and 1699 cm^{-1} events) with respect to SF-MeOH. The co-occurrence of the SS and SF fractions could be further evidenced by confocal microscopy (Figure 3C). SF could be directly imaged by Second Harmonic Generation (SHG), whose signal is a characteristic feature of the co-alignment of non-centrosymmetric protein secondary structures (α-helices and β-sheets).

To ascertain the presence of SS in SS@SF foams, SS was grafted with RITC dye and subsequently coated onto the surface of MeOH-treated SF foams by immersion for 2 h. The left panel in Figure 3C was obtained by exciting SF-MeOH samples under a confocal microscope at λ_{ex} = 880 nm and collecting the emission signal at λ_{em} = 440 nm, corresponding to the frequency doubling characteristic of SHG. In the right panel of Figure 3C, SS@SF foam displays SHG signal and RITC fluorescence endowed by the SF crystallites and RITC-grafted SS, respectively, suggesting extensive coating of the former. The two channels' pixel intensity at each plane correlate positively (SHG signal from the β-sheet domains of SF and fluorescence from the RITC-SS moiety) as determined from the co-localization analysis using FIJI software.[37] Data correlation was analyzed after an automated thresholding of both channels using the Costes algorithm (SHG/SF max. threshold = 34 and RITC-SS max. threshold = 31 for 256 gray levels).[34] Figure 3D depicts the two-dimensional (2D) correlation heatmap obtained from co-localization analysis. Pearson's correlation coefficient (ranging from -1 for anti-correlation to 1 for perfect correlation) was equal to 0.55, suggesting a strong correlation between the two

channels, eventually affected by the signal intensity difference between the two channels.[36] Manders' tM1 parameter[35] was equal to 0.61, which indicates the high fraction of SF voxels (above threshold) that are co-localized with SS voxels (above threshold). These results confirm that after automatic thresholding (that eliminates the large number of background voxels) there is an extensive coverage of SF structures by SS.

To understand the ability of SS@SF dermal patches to favor exudate wicking from the wound surface, we designed a setup that mimics the wound exudate formation at the wound/patch interface (Figure S1 in the Supporting Information). Hydrated SS@SF foams were placed over a silicone surface used to mimic the wound/skin surface. A 3µL.s^{-1} inflow of water—used as a simplified exudate liquid—was delivered under the patch by a needle crossing the silicone substrate. After the water filled the pores of the macroporous silk patch, a water cap accumulated above its surface, away from the hypothetical wound site. Figure 3E depicts the water cap profile measured above the patch surface. The low contact angles formed and the fact that the water cap occupies the full upper surface of the foam suggest the material is hydrophilic. These results are in good agreement with the hydrophilic nature of SS covering the hydrophobic β-sheets[45,46] that compose the core fraction composes of SF. The volume of the water cap was calculated from the cap height and radius (see eq. S1 in Supporting Information) detected by video analysis using FIJI software. Two regimes are observed from the plot of the water cap volume as a function of time (Figure 3F). The first, between the beginning of water injection (0*s*) and the initial appearance of the water cap above the foam (25*s*) corresponds to the filling of the sample pores. Multiplying the inflow rate (3 µL.s^{-1}) by the time (25*s*) yields 75 µL. This value is coherent with the foam total volume (*ca*. 81 µL) and the low mass fraction of SF foams (*ca*. 5 wt.%). The SS@SF macroporous silk foams were thus capable of retaining close to 20 times

more water than the foams' dry weight, an interesting property in wound exudate clearance. From 25*s* onwards, the water cap volume grew linearly until the foam detached from the substrate. The water cap growth rate measured, 1.9 $\mu L.s^{-1}$, indicates that most of the exudate production (over 60%) was effectively extracted from the wound model to the outer surface of the patch. Contrary to SS@SF dermal patches, SF-MeOH samples did not promote water wicking using the same setup and water inflow conditions. The hydrated SF-MeOH samples detached from the PDMS surface from the initial moments of water injection as depicted in Figure S2. The intrinsic hydrophobic character of the SF β-sheets induced by the methanol is particularly effective to stabilize the SF foams but prevented the effective wetting of the patch pores. These results highlight the key role of the SS coating on the patches internal porosity to modulate their ability to remove the exudate from wounds.

One aspect that is often disregarded when considering antibacterial dermal patches is that of their deformability under the strain imposed by the skin. In order to develop antibacterial dermal patches that display optimal adhesion to the wound, the mechanical solicitation induced by the deformation of skin should be followed by the dermal patch to avoid detachment. We performed a compliance test for both MeOH-treated SF and SS@SF hydrated foams adhered on the surface of silicone substrates that were stretched to mimic the maximum stretch ratio of skin (*c.a.* 20-30% depending on the body area in human skin[47]) (Figure 4A). The stretch ratio of the foams was plotted against the silicone stretch ratio to extract the compliance of the hydrated foams under strain induced by the silicone substrate. Regardless of freezing rate and SS-coating, all foams exhibited good compliance when silicone was stretched to 10%. Above this value foams exhibited lower stretch ratio than the substrate. When the silicone was stretched to 25% (close to the maximum surface strain experienced by arm skin[47]), the foams were stretched by

approximately 14%. We performed statistical analysis of the significance between average ϵ_{patch} values for samples obtained with similar freezing rates (1, 10 and 100 °C min^{-1}) with and without SS at 10, 20 and 30% (Figure 4B). P-values were consistently above 0.05 (noted *ns*) suggesting the addition of SS did not modify significantly the compliance of the patches on a silicone stretching model. Although literature lacks the data of the dermal patches' ability to accommodate the skin (or a skin model) stretching without detachment, we believe such measurement is central to provide an idea of the conditions under which the patches can be applied without mechanical stabilization by adhesive straps. Although the patches do not deform to the same extent as the skin model beneath, the SF-based patches did not detach when the substrate was stretched up to 30%, suggesting their suitability to accommodate normal mechanical solicitation induced by skin without requiring a supplementary protective layer (e.g., adhesive straps).

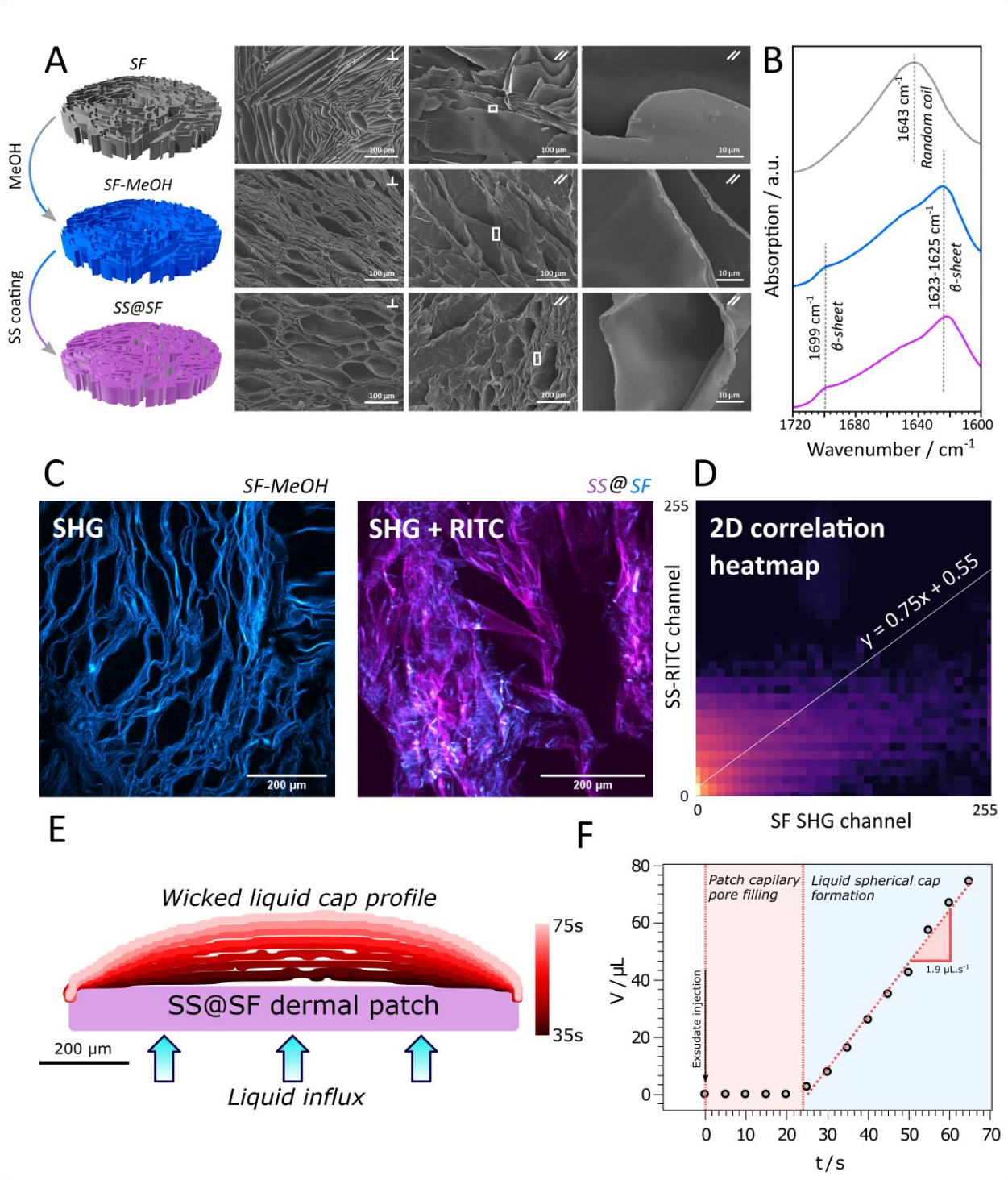

Figure 3 The modification of SF with SS following MeOH treatment step preserves the morphology and mechanical properties of the foams, while promoting a major change in the protein's proportion of β-sheet. (A) Scheme of SF-based foams modification process and

corresponding SEM images at 5.0 wt. % obtained at 10 °C.min^{-1}. Imaged planes denoted (⊥) are perpendicular to the ice crystal growth direction and planes denoted (∥) are parallel to the ice growth direction. (B) ATR/FTIR spectra of amide I band region of SF foams after ice-templating (grey line), after MeOH treatment (blue line) and following SS deposition (magenta line). (C) Confocal microscopy of SF-MeOH (left panel) and SS@SF (right panel) foams fabricated at 10 °C.min^{-1}. Scale bar, 100 μm. Blue channel was obtained from second harmonic generation (SHG) signal from the β-sheet domains in SF. Magenta channel codes for SS grafted with RITC dye. (D) 2D correlation heatmap between blue (SF) and magenta (SS) channel. (E) Profile of water cap above SS@SF patch obtained at 10 °C.min^{-1} in wicking experiments. (F) Wicked water cap volume as function of time.

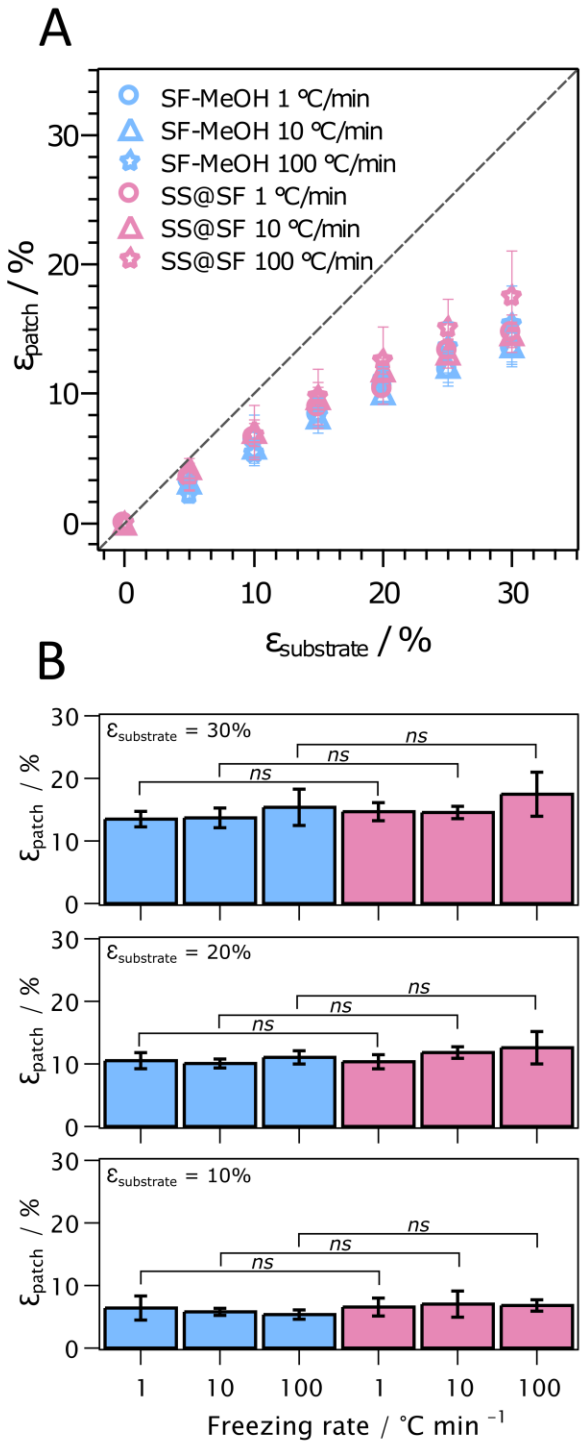

Figure 4 The modification of SF foams with SS preserves the compliance properties of the foams. (A) Compliance test of SF-MeOH and SS@SF, fabricated at 1 (circle symbols), 10 (triangle symbols) and 100 °C.min^{-1} (star symbols) cooling rate. Blue and magenta symbols

represent SF-MeOH and SS@SF, respectively. (B) Column charts depicting the statistical analysis of SF-MeOH and SS@SF samples prepared at similar freezing rate (1, 10 and 100 °C min^{-1}) at patch deformation equal to 10, 20 and 30%.

Antibacterial activity. To ascertain their applicability as antibacterial patches, SF foams were loaded with Rif dissolved in MeOH (Figure 5A). In this first step the loading efficiency (*ca*. 17.5 $mg.g^{-1}$) was independent of the freezing rate (yellow bars, Figure 5B), suggesting that different cooling rates—and thus different pore sizes—did not affect the materials' capacity to retain the antibiotic drug. These results are compatible with drug retention capacity determined by the SF weight rather than the materials' porosity or surface. On the contrary, after soaking the foams in an aqueous solution containing SS (SS@SF/Rif)—to remove residual MeOH and cover of the SF foam with SS—the drug loading varied from 6.2 $mg.g^{-1}$ when foams were prepared at 1 °$C.min^{-1}$ to 3.3 $mg.g^{-1}$ when foams were prepared at 100 °$C.min^{-1}$ (red bars, Figure 5B). In parallel, SF-MeOH/Rif foams were soaked in water for 2h to remove MeOH (SF/Rif) and to act as a control (blue bars, Figure 5B). These materials displayed smaller drug retention (*c.a.* 2 $mg.g^{-1}$) irrespective of the freezing conditions. Comparing the drug retention results from SS@SF/ Rif and SF/Rif shows the importance of the SS coating step. It allows to *i*) minimize the drug leaching when compared to non-coated samples and *ii*) adjust the drug loading according with the freezing rates. Soaking the SF-MeOH/Rif foams in aqueous SS solution can be seen as a competition between two processes: Rif leaching from the matrix and the deposition of SS on the matrix surface. These two processes lead to opposite outcomes, one limiting the total amount of Rif retained in the matrix and the other favoring its retention due to the presence of SS at the

surface of the foams, respectively. In this scenario, bigger pores in the foam may favor the transport and deposition of the SS within the SF porous matrices and thus lead to a more effective retention of the drug within the foams. On the contrary, materials prepared at increasing freezing rates—that result in smaller pores (Figure 2B) and consequently in higher surface area—may require a longer period for full SS coating of the foam's internal surface, allowing enough time for drug desorption. Foams directly soaked in water retain the lowest concentration of Rif due to the absence of competition with the SS deposition. Regardless of the presence of sericin coating all foams kept releasing Rif for at least 96 h. The release profiles of rifamycin from SS@SF/Rif foams (Figure 5C) in solution are similar, suggesting the freezing rate plays an important role in the materials loading capacity but a rather moderate effect on the antibiotic release profile. On the contrary, SF/Rif materials (not exposed to SS), whose Rif loading capacity is independent from the freezing rate, display rather different release profiles, with samples frozen at 1°C.min^{-1} releasing Rif much faster than samples frozen at 100 °C.min^{-1}. Given the similar Rif content within the SF/Rif foams (Figure 5B), tuning freezing rate during foam fabrication allows to regulate the release kinetics in aqueous media (Figure 5D). This effect seems negligible in the case of SS@SF/Rif foams, where no visible difference is observed in the release profiles as a function of the freezing rate and the release kinetics seem to be controlled by the SS layer.

We applied three common drug release models—Higuchi, Korsmeyer-Peppas and Weibull—to describe the data from drug release experiments in solution. The different fitting results, presented in Figure S3 and in Table S1of the Supporting Information section, suggest that the Weibull model (Equation 1) describes the release profile more accurately than the other models considered (Table 1):

$$M_t = M_\infty \left(1 - e^{(-at)^b}\right) \quad \text{(Eq. 1)}$$

where M_t corresponds to the cumulative release of the active principle at time *t*, M_∞ corresponds to total amount of drug released and, *a* and *b* correspond to empirical constants of the Weibull function. The ability of the Weibull function to accurately describe the Rif release results from silk based foams is comforted by the Monte Carlo analysis of the release profiles performed by Kosmidis and co-authors.[48] They demonstrated that this function was suitable to describe the release profiles regardless of the initial concentration of the drug. Beyond that, their findings allow to ascribe some physical sense to parameters *a* and *b*; the first being dependent on the specific surface of the material—and inversely proportional to the release half-time—and the latter depending mostly on the molecular interactions between drug molecules but also on the specific surface of the materials.

In all the materials studied here, regardless of the freezing velocity during their elaboration and regardless of the deposition or not of a SS layer, $b \leq 0.75$, indicating a Fickian diffusion-dominated release.[49] SS@SF/Rif foams' *a* and *b* Weibull parameters presented little variation as a function of the freezing rate, suggesting the deposition of the SS coating dominates the release mechanism. Increasing freezing rate from 1 to 100 °C.min^{-1} in SF/Rif foams, however, resulted in an dramatic reduction of the *a* parameter (from 0.156 to 0.040), corresponding to increasingly large release half-time. The smaller pore section observed for high freezing rate foams could limit the diffusion of Rif out of foams and therefore delay the release kinetics, even if these are expected to display a more extensive specific surface. Also, due to the narrower pores, a potential swelling of the SF matrix walls could narrow further the channels of the materials,

resulting in clogged pores that could slow down the diffusion of Rif from the foam to the surrounding solution. The changes observed in the *b* parameter suggest the intermolecular interactions of the Rif molecules may differ between SF/Rif foams prepared at different freezing rates. It is however difficult to draw a solid conclusion here since tis parameter is also expected to depend on the sample surface area, which is expected to change with the freezing conditions.

To explore the role of the proteins' dissolution on drug release, we conducted protein quantification in the liquid medium for SF/Rif and SS@SF/Rif during 96 h. For SS@SF foams, the dissolution of silk proteins during release experiments displayed a similar profile as Rif the release (Figure S4 in the Supporting Information), suggesting the relevance of the freezing rate on antibiotic release kinetics. In parallel, the release of SF from SF/Rif foams in water—regardless of the freezing rate—suggests that the MeOH treatment limits protein dissolution in solution. Even if the release rate from SS coated foams was faster that uncoated samples in solution, the findings above demonstrate that both SS coating and freezing rate played a positive role in improving Rif initial loading within foams. Both parameters can thus act as an effective lever to modulate indirectly the release profile from SF-based foams.

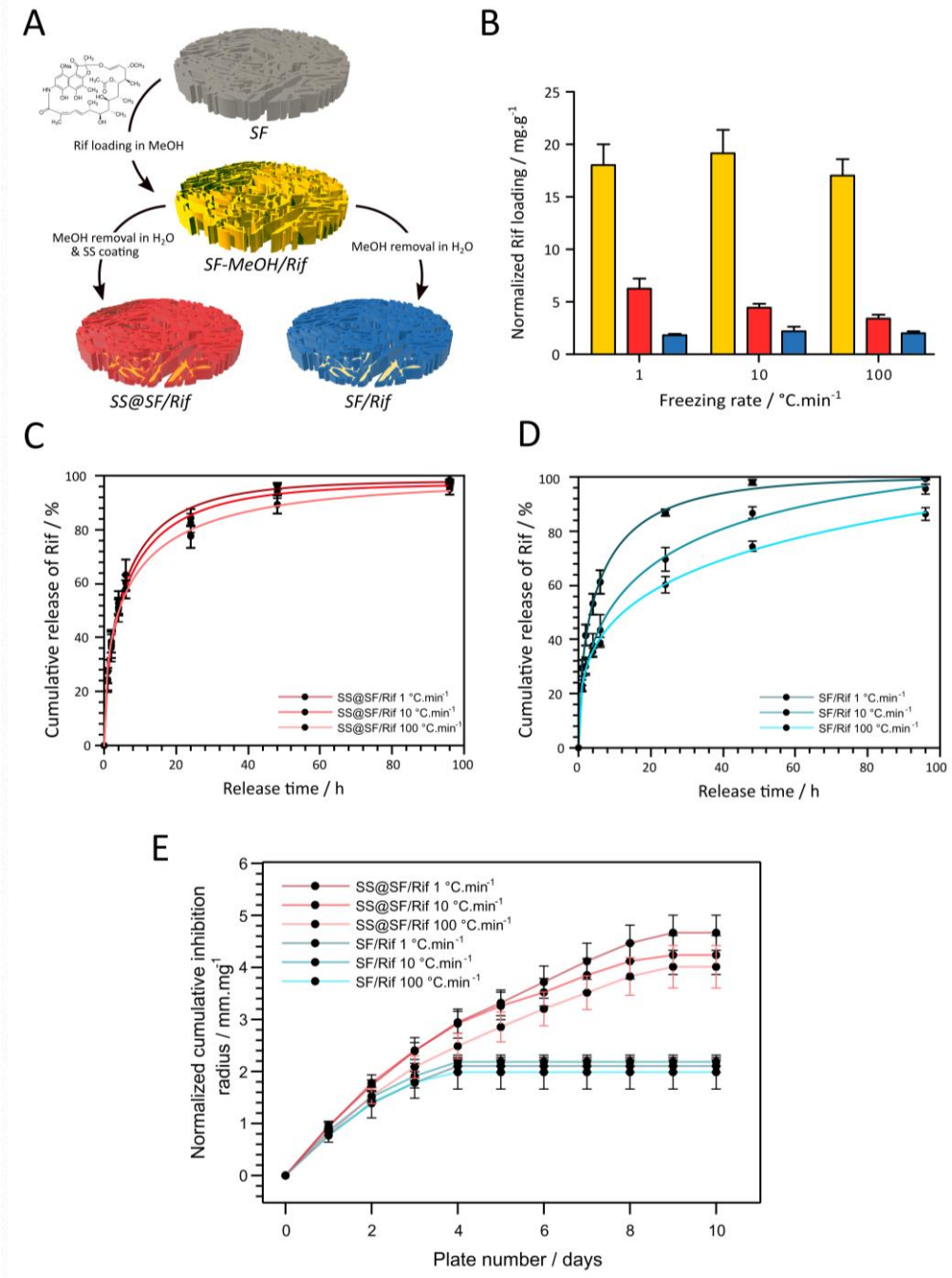

Figure 5 Antibiotic release behavior in SS@SF foams is dictated by SS coating. (A) Rif loading process in SF foams: after loading, foams (yellow) are soaked for 2 hours in a SS aqueous solution leading to simultaneous deposition of sericin and removal of remaining MeOH (red foam) or just soaked in water as a control to remove remaining MeOH (blue foam). (B) Initial Rif loading in SF-MeOH/Rif (yellow column), after soaking SF-MeOH/Rif for 2 h in SS solution

(red column, SS@SF/Rif), and after soaking SF-MeOH/Rif for 2 h in H_2O (dark blue column, SF/Rif) as function of freezing rate. (C, D) Rif release profiles in aqueous media from SS@SF/Rif (left panel) and SF/Rif (right panel). Release profiles are fitted to the Weibull function. (E) *Kirby–Bauer* test of foams of SS@SF/Rif (red tones) and SF/Rif (blue tones) prepared at 1, 10 and 100 °C.min^{-1} showing the cumulative inhibition zones' radius at each plate. Blue and red lines represent release from SF/Rif and SS@SF/Rif, respectively. Darker lines correspond to foams prepared at 1 °C.min^{-1}, intermediate lines to 10 °C.min^{-1} and lighter lines to 100 °C.min^{-1}. Lines between experimental data points are exclusively a guide to the eye.

Finally, we performed Kirby–Bauer tests[50] to validate the antibacterial behavior of Rif against *S. aureus* (Figure 5E). The diameter of the inhibition zone is the main indicator to describe the antibacterial activity of the materials. Compared to previous studies in solution, here Rif had to diffuse through the agar gel, and bacteria growth inhibition required that antibiotic concentration be larger than its Minimum Inhibitory Concentration (MIC). Thus, the kinetics of Rif release observed from the disc method were expected to be delayed compared to spectrophotometric titration of antibiotics released in solution. Moreover, contrary to the Rif release results in solution, SS@SF/Rif foams exhibited a longer Rif release period (~ 9 days) compared to that from SF/Rif foams (~ 4 days), supporting the choice of SS coating on the SF foams. We also found that increasing the freezing rate during foam preparation led to lower cumulative inhibition radius and thus less Rif release. Besides, variation of the freezing rate failed to tune Rif release kinetics on solid agar plate for SF/Rif foams in contrast to what was observed in solution.

Table 1. Weibull fitting parameter of Rif release profiles for SF/Rif and SS@SF/Rif foams.

Ice-templating conditions of Rif-loaded foams	Weibull model, $M_t = M_\infty(1 - e^{(-at)^b})$		
	a	*b*	r^2
1 °C.min^{-1} SS@SF/Rif	0.144 ± 0.008	0.593 ± 0.03	0.997
10 °C.min^{-1} SS@SF/Rif	0.126 ± 0.007	0.569 ± 0.03	0.997
100 °C.min^{-1} SS@SF/Rif	0.111 ± 0.005	0.471 ± 0.02	0.998
1 °C.min^{-1} SF/Rif	0.156 ± 0.005	0.565 ± 0.02	0.999
10 °C.min^{-1} SF/Rif	0.066 ± 0.004	0.545 ± 0.02	0.997
100 °C.min^{-1} SF/Rif	0.040 ± 0.003	0.444 ± 0.02	0.995

Overall, it was possible to obtain SF foams with oriented pores whose size decreased with increasing freezing rate. However, after treatment with MeOH—added for SF matrix stabilization purposes—in the presence of Rif, freezing rate played a negligible role both on the foam stability in aqueous solution, and on the antibiotic loading. Freezing rate did have an impact on the Rif release kinetics in solution, but not when the release was conducted in solid form. We hypothesize that the different impact of the freezing rate on the release kinetics of Rif from SF/Rif patches in solution and in agar can be ascribed to the hydrophobic nature of non-coated SF. Foams prepared at lower freezing rates display wider pores—which are easier to wet—leading to increased release kinetics. Conversely, foams with narrower pores—obtained at higher freezing rates—are more difficult to wet and the transport of Rif between the foam and the solution occurs in a less effective manner. On agar plates these differences are less important since the effective exchange surface is determined by the direct contact between the foams and the agar. This difference in effective exchange surface could also account for the extended

release period found on the Kirby Bauer plates as compared to the release in solution. Deposition of a SS coating to form a reconstituted silk material led to highest drug loading for the lowest freezing rate, *i.e*. the largest pores, suggesting some influence of SS diffusion on the coating extent. The addition of SS accounts for enhanced hydrophilicity of the foams, reducing the disparities in Rif release due to impaired wetting in solution.

It is well-established that, for wound repair, up to 10 days are needed for the reconstruction of connective tissue and new blood vessel networks that are essential in the healing process.[51] During this period, prevention from bacterial infection is critical. The above results show that SS@SF antibacterial patches achieved ~ 9 days' continuous release of antibiotics, clearly meeting this demand. Moreover, the ability to produce aligned macropores perpendicular to the patches' surface promoted efficient water wicking properties which may prove central for its application. Foot ulcer wounds from diabetic patients infected with *S. aureus* were reported as having the highest exudate rate from a number of other exudate-forming wounds.[52] The case study evaluated 3 patients with the same pathology and determined that the average exudate formation rate from the ulcers was 2.8 $mL.cm^{-2}.day^{-1}$. Each one of the 1 mm-high SS@SF patch reported here can accommodate a liquid exudate rate close to 170 $mL.cm^{-2}.day^{-1}$ (1.9 $\mu L.s^{-1}$ per sample surface area, ca. 0.95 cm^2) equivalent to over 60 days of exudate production. This liquid wicking capacity comforts the long-term application of the SS@SF patches as determined by the antibiotic release studies that suggests their active drug release for 9 days.

CONCLUSIONS

Combining top-down and bottom-up design approaches resulted in macroporous silk materials that recapitulate the topological arrangement of native silk with an inner phase of SF

surrounded by a sheath of SS. Such combination enabled us to tune the foams' surface and bulk properties, and yield a re-engineered material with long-term controlled drug release.

Stabilization of SF foams with MeOH allowed to modulate SF solubility without a covalent crosslinking step to obtain stable, hydrated foams with controlled macroporosity. SS coating favored the retention of higher antibiotic loading as compared to non-coated foams, resulting in materials that exhibit antibacterial properties in a solid hydrated environment beyond 1 week. Moreover, we show that coating SF macroporous scaffolds with SS leads to macroporous silk matrices that act as liquid wicking materials able to extract the fluids generated between the patch in a simple skin model.

The combination of controlled morphology in the absence of crosslinking agents, high loading capacity, liquid wicking properties, and controlled release of antimicrobial loading configure an outstanding material with clear interest as antibacterial dressing for clinical applications.

The design-oriented strategy introduced here takes advantage of the unique intrinsic organization of native silk. It encompasses the controlled removal of the outer structure of the raw natural material and the judicious redesign of its core structure to re-build an engineered biomaterial with new functionalities. This new approach may extend to design other biomaterials with application in the clinical context requiring a combination of liquid transport, biocompatibility, and controlled release properties, but could virtually be also of pivotal interest for many other areas where fluid transport is critical.

ASSOCIATED CONTENT

Supporting Information

Water wicking analysis setup (Fig. S1). Image sequence of water wicking analysis of SF-MeOH porous samples (Fig. S2). Normalized rifamycin and total protein release profiles from silk-based foams during drug release test (Fig. S3). Model fitting curves (Higuchi, Korsmeyer-Peppas and Weibull) of rifamycin release from SF/Rif foams (Fig. S4). Rifamycin release fitting parameters for Higuchi, Korsmeyer-Peppas and Weibull models (Table S1).

AUTHOR INFORMATION

Corresponding Authors

*francisco.fernandes@sorbonne-universite.fr and *vbermude@utad.pt

Author Contributions

The manuscript was written through contributions of all authors. All authors have given approval to the final version of the manuscript.

ACKNOWLEDGMENT

This research was funded by Fundação para a Ciência e a Tecnologia (FCT) (UID/QUI/00686/2019, UID/QUI/00686/2019). FCT and Égide are acknowledged for Pessoa/Hubert Curien 2017/2018 project “Redesigning silk fibroin-based composites via freeze-casting” (Ref. 3775/38003ZHR). KQ acknowledges funding from the China Scholarship Council, PhD grant n. 201606230232. R.F.P. Pereira thanks FCT-UM for the contracts in the scope of Decreto-Lei 57/2016 and 57/2017.

REFERENCES

(1) Li, J.; Bao, Q.; Chen, S.; Liu, H.; Feng, J.; Qin, H.; Li, A.; Liu, D.; Shen, Y.; Zhao, Y.; Zong, Z. Different Bone Remodeling Levels of Trabecular and Cortical Bone in Response to Changes in Wnt/β-Catenin Signaling in Mice. *J. Orthop. Res.* **2017**, *35* (4), 812–819.

(2) Paris, O.; Fritz-Popovski, G.; Van Opdenbosch, D.; Zollfrank, C. Recent Progress in the Replication of Hierarchical Biological Tissues. *Adv. Funct. Mater.* **2013**, *23* (36), 4408–4422.

(3) Wang, J. C.; Wang, C. Y.; Zhu, C. Q.; Hu, S. Borehole Image-Based Evaluation of Coral Reef Porosity Distribution Characteristics. *Mar. Georesources Geotechnol.* **2017**, *35* (7), 1008–1017.

(4) Kröger, N. Prescribing Diatom Morphology: Toward Genetic Engineering of Biological Nanomaterials. *Curr. Opin. Chem. Biol.* **2007**, *11* (6), 662–669.

(5) Mann, S.; Ozin, G. A. Synthesis of Inorganic Materials with Complex Form. *Nature* **1996**, *382* (6589), 313–318.

(6) Rieu, C.; Parisi, C.; Mosser, G.; Haye, B.; Coradin, T.; Fernandes, F. M.; Trichet, L. Topotactic Fibrillogenesis of Freeze-Cast Microridged Collagen Scaffolds for 3D Cell Culture. *ACS Appl. Mater. Interfaces* **2019**, *11* (16), 14672–14683.

(7) Francis, N. L.; Hunger, P. M.; Donius, A. E.; Riblett, B. W.; Zavaliangos, A.; Wegst, U. G. K.; Wheatley, M. a. An Ice-Templated, Linearly Aligned Chitosan-Alginate Scaffold for Neural Tissue Engineering. *J. Biomed. Mater. Res. - Part A* **2013**, *101* (12), 3493–3503.

(8) Yin, K.; Divakar, P.; Wegst, U. G. K. Freeze-Casting Porous Chitosan Ureteral Stents for Improved Drainage. *Acta Biomater.* **2019**, *84*, 231–241.

(9) Wegst, U. G. K.; Schecter, M.; Donius, A. E.; Hunger, P. M. Biomaterials by Freeze Casting. *Philos. Trans. A. Math. Phys. Eng. Sci.* **2010**, *368* (1917), 2099–2121.

(10) Qin, K.; Parisi, C.; Fernandes, F. M. Recent Advances in Ice Templating: From Biomimetic Composites to Cell Culture Scaffolds and Tissue Engineering. *J. Mater. Chem. B* **2021**, *9* (4), 889–907.

(11) Mandal, B. B.; Gil, E. S.; Panilaitis, B.; Kaplan, D. L. Laminar Silk Scaffolds for Aligned Tissue Fabrication. *Macromol. Biosci.* **2013**, *13* (1), 48–58.

(12) Oliveira, A. L.; Sun, L.; Kim, H. J.; Hu, X.; Rice, W.; Kluge, J.; Reis, R. L.; Kaplan, D. L. Aligned Silk-Based 3-D Architectures for Contact Guidance in Tissue Engineering. *Acta Biomater.* **2012**, *8* (4), 1530–1542.

(13) Christoph, S.; Hamraoui, A.; Bonnin, E.; Garnier, C.; Coradin, T.; Fernandes, F. M. Ice-Templating Beet-Root Pectin Foams: Controlling Texture, Mechanics and Capillary Properties. *Chem. Eng. J.* **2018**, *350* (February), 20–28.

(14) Zhang, W.; Chen, L.; Chen, J.; Wang, L.; Gui, X.; Ran, J.; Xu, G.; Zhao, H.; Zeng, M.; Ji, J.; Qian, L.; Zhou, J.; Ouyang, H.; Zou, X. Silk Fibroin Biomaterial Shows Safe and Effective Wound Healing in Animal Models and a Randomized Controlled Clinical Trial. *Adv. Healthc. Mater.* **2017**, *6* (10), 1–16.

(15) Gil, E. S.; Panilaitis, B.; Bellas, E.; Kaplan, D. L. Functionalized Silk Biomaterials for Wound Healing. *Adv. Healthc. Mater.* **2013**, *2* (1), 206–217.

(16) Min, B. M.; Jeong, L.; Lee, K. Y.; Park, W. H. Regenerated Silk Fibroin Nanofibers: Water Vapor-Induced Structural Changes and Their Effects on the Behavior of Normal Human Cells. *Macromol. Biosci.* **2006**, *6* (4), 285–292.

(17) Sugihara, A.; Sugiura, K.; Morita, H.; Ninagawa, T.; Tubouchi, K.; Tobe, R.; Izumiya, M.; Horio, T.; Abraham, N. G.; Ikehara, S. Promotive Effects of a Silk Film on Epidermal Recovery from Full-Thickness Skin Wounds. *Proc. Soc. Exp. Biol. Med.* **2008**, *225* (1), 58–64.

(18) Clemens, M. W.; Downey, S.; Agullo, F.; Lehfeldt, M. R.; Kind, G. M.; Palladino, H.; Marshall, D.; Jewell, M. L.; Mathur, A. B.; Bengtson, B. P.; Clemens, M. W. Clinical Application of a Silk Fibroin Protein Biologic Scaffold for Abdominal Wall Fascial Reinforcement. *Plast. Reconstr. Surg. - Glob. Open* **2014**, *2* (11), 1–10.

(19) Pecquet, C. Allergic Reactions to Insect Secretions. *European Journal of Dermatology*. November 2013, pp 767–773.

(20) Kunz, R. I.; Brancalhão, R. M. C.; Ribeiro, L. D. F. C.; Natali, M. R. M. Silkworm Sericin: Properties and Biomedical Applications. *Biomed Res. Int.* **2016**, *2016* (8175701), 1–19.

(21) Gilotra, S.; Chouhan, D.; Bhardwaj, N.; Nandi, S. K.; Mandal, B. B. Potential of Silk Sericin Based Nanofibrous Mats for Wound Dressing Applications. *Mater. Sci. Eng. C* **2018**, *90*, 420–432.

(22) Chen, C. S.; Zeng, F.; Xiao, X.; Wang, Z.; Li, X. L.; Tan, R. W.; Liu, W. Q.; Zhang, Y. S.; She, Z. D.; Li, S. J. Three-Dimensionally Printed Silk-Sericin-Based Hydrogel Scaffold: A Promising Visualized Dressing Material for Real-Time Monitoring of Wounds. *ACS Appl. Mater. Interfaces* **2018**, *10* (40), 33879–33890.

(23) Mandal, B. B.; Priya, A. S.; Kundu, S. C. Novel Silk Sericin/Gelatin 3-D Scaffolds and 2-D Films: Fabrication and Characterization for Potential Tissue Engineering Applications. *Acta Biomater.* **2009**, *5* (8), 3007–3020.

(24) Zhang, Y.-Q. Applications of Natural Silk Protein Sericin in Biomaterials. *Biotechnol. Adv.* **2002**, *20* (2), 91–100.

(25) Thurber, A. E.; Omenetto, F. G.; Kaplan, D. L. In Vivo Bioresponses to Silk Proteins. *Biomaterials*. Elsevier Ltd December 2015, pp 145–157.

(26) Rockwood, D. N.; Preda, R. C.; Yücel, T.; Wang, X.; Lovett, M. L.; Kaplan, D. L. Materials Fabrication from Bombyx Mori Silk Fibroin. *Nat. Protoc.* **2011**, *6* (10), 1612–1631.

(27) Maslow, M. J.; Portal-Celhay, C. Rifamycins. In *Mandell, Douglas, and Bennett's Principles and Practice of Infectious Diseases*; Elsevier, 2019; pp 337–349.

(28) Sarheed, O.; Ahmed, A.; Shouqair, D.; Boateng, J. Antimicrobial Dressings for Improving Wound Healing. In *Wound Healing - New insights into Ancient Challenges*; InTech, 2016.

(29) Helary, C.; Abed, A.; Mosser, G.; Louedec, L.; Letourneur, D.; Coradin, T.; Giraud-Guille, M. M.; Meddahi-Pelle, A. Evaluation of Dense Collagen Matrices as Medicated Wound Dressing for the Treatment of Cutaneous Chronic Wounds. *Biomater. Sci.* **2015**, *3*, 373–382.

(30) Panasci, K. Burns and Wounds. In *Acute Care Handbook for Physical Therapists (Fourth Edition)*; 2014; pp 283–311.

(31) Kamel, R. A.; Ong, J. F.; Eriksson, E.; Junker, J. P. E.; Caterson, E. J. Tissue Engineering of Skin. *Journal of the American College of Surgeons*. Elsevier Inc. 2013, pp 533–555.

(32) Smith, D. M.; Snow, D. E.; Rees, E.; Zischkau, A. M.; Hanson, J. D.; Wolcott, R. D.; Sun, Y.; White, J.; Kumar, S.; Dowd, S. E. Evaluation of the Bacterial Diversity of Pressure Ulcers Using BTEFAP Pyrosequencing. *BMC Med. Genomics* **2010**, *3* (1), 41.

(33) Gianino, E.; Miller, C.; Gilmore, J. Smart Wound Dressings for Diabetic Chronic Wounds. *Bioengineering* **2018**, *5* (3), 51.

(34) Costes, S. V.; Daelemans, D.; Cho, E. H.; Dobbin, Z.; Pavlakis, G.; Lockett, S. Automatic and Quantitative Measurement of Protein-Protein Colocalization in Live Cells. *Biophys. J.* **2004**, *86* (6), 3993–4003.

(35) Manders, E. M. M.; Verbeek, F. J.; Aten, J. A. Measurement of Co-localization of Objects in Dual-colour Confocal Images. *J. Microsc.* **1993**, *169* (3), 375–382.

(36) Dunn, K. W.; Kamocka, M. M.; McDonald, J. H. A Practical Guide to Evaluating Colocalization in Biological Microscopy. *Am. J. Physiol. - Cell Physiol.* **2011**, *300* (4), 723–742.

(37) Schindelin, J.; Arganda-Carreras, I.; Frise, E.; Kaynig, V.; Longair, M.; Pietzsch, T.; Preibisch, S.; Rueden, C.; Saalfeld, S.; Schmid, B.; Tinevez, J. Y.; White, D. J.; Hartenstein, V.; Eliceiri, K.; Tomancak, P.; Cardona, A. Fiji: An Open-Source Platform for Biological-Image Analysis. *Nature Methods*. July 2012, pp 676–682.

(38) Jin, H. J.; Park, J.; Karageorgiou, V.; Kim, U. J.; Valluzzi, R.; Cebe, P.; Kaplan, D. L. Water-Stable Silk Films with Reduced β-Sheet Content. *Adv. Funct. Mater.* **2005**, *15* (8), 1241–1247.

(39) Lu, Q.; Hu, X.; Wang, X.; Kluge, J. A.; Lu, S.; Cebe, P.; Kaplan, D. L. Water-Insoluble Silk Films with Silk I Structure. *Acta Biomater.* **2010**, *6* (4), 1380–1387.

(40) Lu, S.; Wang, X.; Lu, Q.; Zhang, X.; Kluge, J. A.; Uppal, N.; Omenetto, F.; Kaplan, D. L. Insoluble and Flexible Silk Films Containing Glycerol. *Biomacromolecules* **2010**, *11* (1), 143–150.

(41) Tsukada, M.; Freddi, G.; Monti, P.; Bertoluzza, A.; Kasai, N. Structure and Molecular Conformation of Tussah Silk Fibroin Films: Effect of Methanol. *J. Polym. Sci. Part B Polym. Phys.* **1995**, *33* (14), 1995–2001.

(42) Chen, X.; Shao, Z.; Marinkovic, N. S.; Miller, L. M.; Zhou, P.; Chance, M. R. Conformation Transition Kinetics of Regenerated Bombyx Mori Silk Fibroin Membrane Monitored by Time-Resolved FTIR Spectroscopy. *Biophys. Chem.* **2001**, *89* (1), 25–34.

(43) Hu, X.; Kaplan, D.; Cebe, P. Determining Beta-Sheet Crystallinity in Fibrous Proteins by Thermal Analysis and Infrared Spectroscopy. *Macromolecules* **2006**, *39* (18), 6161–6170.

(44) Barth, A. Infrared Spectroscopy of Proteins. *Biochim. Biophys. Acta - Bioenerg.* **2007**, *1767* (9), 1073–1101.

(45) Wang, L.; Xie, H.; Qiao, X.; Goffin, A.; Hodgkinson, T.; Yuan, X.; Sun, K.; Fuller, G. G. Interfacial Rheology of Natural Silk Fibroin at Air/Water and Oil/Water Interfaces. *Langmuir* **2012**, *28* (1), 459–467.

(46) Lefèvre, T.; Rousseau, M. E.; Pézolet, M. Protein Secondary Structure and Orientation in Silk as Revealed by Raman Spectromicroscopy. *Biophys. J.* **2007**, *92* (8), 2885–2895.

(47) Maiti, R.; Gerhardt, L. C.; Lee, Z. S.; Byers, R. A.; Woods, D.; Sanz-Herrera, J. A.; Franklin, S. E.; Lewis, R.; Matcher, S. J.; Carré, M. J. In Vivo Measurement of Skin Surface Strain and Sub-Surface Layer Deformation Induced by Natural Tissue Stretching. *J. Mech. Behav. Biomed. Mater.* **2016**, *62*, 556–569.

(48) Kosmidis, K.; Argyrakis, P.; Macheras, P. A Reappraisal of Drug Release Laws Using Monte Carlo Simulations: The Prevalence of the Weibull Function. *Pharm. Res.* **2003**, *20* (7), 988–995.

(49) Gbureck, U.; Vorndran, E.; Müller, F. A.; Barralet, J. E. Low Temperature Direct 3D Printed Bioceramics and Biocomposites as Drug Release Matrices. *J. Control. Release* **2007**, *122* (2), 173–180.

(50) Kung, M. L.; Lin, P. Y.; Peng, S. W.; Wu, D. C.; Wu, W. J.; Yeh, B. W.; Tai, M. H.; Hung, H. S.; Hsieh, S. Biomimetic Polymer-Based Ag Nanocomposites as a Antimicrobial Platform. *Appl. Mater. Today* **2016**, *4*, 31–39.

(51) Barnes, L. A.; Marshall, C. D.; Leavitt, T.; Hu, M. S.; Moore, A. L.; Gonzalez, J. G.;

Longaker, M. T.; Gurtner, G. C. Mechanical Forces in Cutaneous Wound Healing: Emerging Therapies to Minimize Scar Formation. *Advances in Wound Care*. Mary Ann Liebert Inc. February 2018, pp 47–56.

(52) Dealey, C.; Cameron, J.; Arrowsmith, M. A Study Comparing Two Objective Methods of Quantifying the Production of Wound Exudate. *J. Wound Care* **2006**, *15* (4), 149–153.